






Please cite the Published Version

Wang, Haoji, Liu, Tongchao , Chen, Hongyi , Mei, Yu, Gao, Jinqiang, Ni, Lianshan, Hong, Ningyun, Huang, Jiangnan, Hu, Xinyu, Deng, Wentao, Zou, Guoqiang, Hou, Hongshuai , Silvester, Debbie S, Banks, Craig E , Ji, Xiaobo and Amine, Khalil  (2025) Multicationic interactions mitigating lattice strain in sodium layered cathodes. Nature Communications, 16. 4409 ISSN 2041-1723

DOI: <https://doi.org/10.1038/s41467-025-59666-6>

Publisher: Nature Publishing Group

Version: Published Version

Downloaded from: <https://e-space.mmu.ac.uk/639845/>

Usage rights:  Creative Commons: Attribution-Noncommercial-No Derivative Works 4.0

Additional Information: This is an Open Access article published in Nature Communications by Springer Nature.

Data Access Statement: Source data: https://static-content.springer.com/esm/art%3A10.1038%2Fs41467-025-59666-6/MediaObjects/41467_2025_59666_MOESM3_ESM.xlsx

Enquiries:

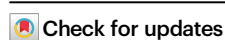
If you have questions about this document, contact openresearch@mmu.ac.uk. Please include the URL of the record in e-space. If you believe that your, or a third party's rights have been compromised through this document please see our Take Down policy (available from <https://www.mmu.ac.uk/library/using-the-library/policies-and-guidelines>)

Multicationic interactions mitigating lattice strain in sodium layered cathodes

Received: 21 August 2024

Accepted: 30 April 2025

Published online: 13 May 2025



Haoji Wang¹, Tongchao Liu²✉, Hongyi Chen¹, Yu Mei^{1,2}, Jinqiang Gao¹, Lianshan Ni¹, Ningyun Hong¹, Jiangnan Huang¹, Xinyu Hu¹, Wentao Deng¹, Guoqiang Zou¹, Hongshuai Hou¹✉, Debbie S. Silvester³, Craig E. Banks⁴, Xiaobo Ji¹✉ & Khalil Amine²✉

Transition-metal (TM) layered oxides have emerged as the primary cathode choice for sodium-ion batteries (SIBs) due to their high energy density and sustainable chemistry using non-critical elements. However, their anisotropic lattice strain and stress accumulation during (de)sodiation lead to severe structural degradation, yet an intrinsic strain-depressant approach remains elusive. Herein, we propose entropy regulation with zero Li/Co usage to mitigate harmful lattice displacements and enhance the electrochemical performance of sodium layered cathodes. Our findings demonstrate that high entropy design effectively inhibits TMO₆ octahedra distortions upon cycling, as evidenced by hard X-ray absorption spectroscopy, greatly reducing near-surface structural deconstruction and interface side reactions. Furthermore, multicationic interactions driven by configurational entropy thermodynamically mitigate the formation of oxygen defects and strengthen ligand-to-metal coordination. The complementarity inherent in charge compensation within complex systems is unveiled and the restrained lattice parameters deviations without interior volume residuals are successfully achieved. As a result, the multicationic cathode exhibits improved cycling stability and Na⁺ diffusion kinetics in both half and full cells. The cathode chemistries outlined here broaden the prospects for lattice engineering to alleviate bulk fatigue and open up the possibility to develop an economically viable layered oxides with long durability.

Sodium layered oxide cathodes, primarily categorized into P2 and O3 type structural configurations, have been extensively investigated as cathode materials for sodium-ion batteries (SIBs), the most promising and sustainable alternative to lithium-ion batteries. O3-type layered cathodes, referred as Na_xTMO₂ (generally with $x > 0.8$), enable a substantial Na-ion (Na⁺) storage within their lattice structure, resulting in a high initial capacity and energy density. However, as conventional intercalation layered oxides, they are inevitably subject to lattice strain

and stress during the removal and insertion of Na⁺ in and out of the host framework¹. This strain primarily stems from the variation in the ionic radius of redox transition metals (TM) and the Coulomb repulsion of oxygen. The former causes a contraction of the transition metal-oxygen octahedron (TMO₆) and a reduction in the lattice parameter $a(b)$, while the latter alters electrostatic interactions (O-O and O-Na-O), leading to significant changes of c -spacing of the lattice, particularly in the high-voltage region where the c -spacing is rapidly

¹College of Chemistry and Chemical Engineering, Central South University, Changsha, China. ²Chemical Sciences and Engineering Division, Argonne National Laboratory, Lemont, IL, USA. ³School of Molecular and Life Sciences, Curtin University, Perth, WA, Australia. ⁴Faculty of Science and Engineering, Manchester Metropolitan University, Manchester, UK. ✉e-mail: liut@anl.gov; xji@csu.edu.cn; amine@anl.gov

collapsed. These anisotropic lattice displacements collectively build up lattice strain, followed by irreversible phase transitions and mechanical degradation in form of microcracks. Despite concerted efforts devoted to mitigating structural degradations, a direct approach to alleviate the continuous accumulation of lattice strain remains elusive.

To address aforementioned issues, the paradigm of configurational entropy regulation emerges as a noteworthy strategy, which reduces the reliance on critical elements and enhances the electrochemical performance of layered cathodes of SIBs. The entropy infusion could increase the solid solubility of the heterogeneous metals within the structure, mitigating the charge ordering and complex structure evolution of layered cathodes². Specifically, contrasting with conventional binary/ternary oxides, which commonly suffer from complex phase transitions and poor capacity retention, the high-entropy O3-type layered oxide cathodes exhibit smooth structure evolutions with smaller lattice parameter changes, which fortify structure stability and suppress irreversible defects of layered cathodes³. However, the current high entropy designs often incorporate costly elements like Li or Co, such as $\text{Na}_{0.9}\text{Li}_{0.1}\text{Ni}_{0.4}\text{Fe}_{0.2}\text{Mn}_{0.44}\text{Ti}_{0.04}\text{Mg}_{0.02}\text{O}_{1.9}\text{F}_{0.1}$ and $\text{NaNi}_{0.12}\text{Cu}_{0.12}\text{Mg}_{0.12}\text{Fe}_{0.15}\text{Co}_{0.15}\text{Mn}_{0.1}\text{Ti}_{0.1}\text{Sn}_{0.1}\text{Sb}_{0.04}\text{O}_2$, due to their ability to stabilize adjacent oxygen layers and enhance electronic conductivity^{4–7}. Consequently, there is a growing consensus to reduce or eliminate the use of Li and Co in cathode materials without compromising performance^{8–10}. Nevertheless, this endeavor faces formidable challenges due to a lack of understanding of the interaction between each element's contribution to capacity and degradation during cycling.

In this work, we conduct a comparative analysis of zero-Li/Co O3-type layered oxides, highlighting the pivotal role of configuration entropy in enhancing cycling stability and mitigating anisotropic lattice displacements. A high configuration entropy leads to disorderly distributed TMO_6 octahedra within TMO_2 slabs, fostering multicationic interactions that alleviate lattice strain and prevent structural degradation. We observe a smooth O3-P3-O3'-O3 phase transition with reduced volume variations and excellent reversibility. Additionally, the highly stable local coordination environment of TM-O octahedra with mitigated oxygen release is confirmed by both experimental and computational characterizations. As a result, the multicationic zero-Li/Co high entropy cathode exhibits a great cycling stability of 94.8% capacity retention after 100 cycles at 1 C (120 mA g^{-1}) and 83.5% capacity retention after 500 cycles at 5 C (600 mA g^{-1}) within the voltage range of 2.0–4.15 V. It also achieves the improved rate performance of 124.2 and 84.3 mAh g^{-1} at 0.1 C (12 mA g^{-1}) and 10 C (1.2 A g^{-1}), respectively. Prototype sodium-ion full cells deliver a specific capacity of -111.7 mAh g^{-1} at 0.5 C (60 mA g^{-1}), with a high capacity retention of 84.9% after 300 cycles, manifesting the bright prospects for practical applications. The strategic implementation of multicationic interactions broadens the perspectives for achieving a highly stable crystal structure and demonstrates the potential for the development of economically feasible layered oxides cathode without compromising the electrochemical prowess.

Results

Strain-depressant cathode structural properties

A group of layered oxide cathodes was fabricated through a simple and scalable high-temperature solid-state reaction. The configuration entropy was regulated by substituting trivalent Fe^{3+} in $\text{NaNi}_{0.35}\text{Mn}_{0.35}\text{Fe}_{0.3}\text{O}_2$ with divalent Cu^{2+} and tetravalent $\text{Ti}^{4+}/\text{Sn}^{4+}$ to form zero-Li/Co $\text{NaNi}_{0.35}\text{Mn}_{0.35}\text{Cu}_{2x}\text{Fe}_{0.3-4x}\text{Ti}_x\text{Sn}_x\text{O}_2$ ($x = 0, 0.03, 0.04, 0.05, 0.06, \text{ and } 0.07$, denoted as NFM, CFTS3, CFTS4, CFTS5, CFTS6, and CFTS7, respectively) layered oxides, in which Cu^{2+} is attempted to compensate for the loss of capacity resulted from the dilution of Fe^{3+} content, and $\text{Ti}^{4+}/\text{Sn}^{4+}$ is applied to stabilize the structural integrity associated with the high bonding energy of Ti-O and Sn-O. The synthesis process is detailed in the Method section. The chemical

compositions were determined by an inductively coupled plasma optical emission spectrometer (ICP-OES). Supplementary Table 1 shows the compositions of the as-prepared samples align with the targeted composition. Thus, theoretical configurational entropy (S_{conf}) values of the systems with the expected composition and elemental valence are calculated to be 1.10, 1.42, 1.47, 1.49, 1.50, and 1.46 R per unit cell for the NFM, CFTS3, CFTS4, CFTS5, CFTS6, and CFTS7 cathodes based on the definition of S_{conf} ¹¹. The detailed calculation process is described in Methods. Among these compositions, CFTS5 and CFTS6 cathodes exhibit the highest entropy values. Furthermore, DFT calculations confirm that the formation energy of alio-/iso-valent cations located in the TM layer is consistently lower than that in the Na layer, suggesting that Cu, Ti, and Sn atoms are preferentially doped into TM layers (Fig. 1c and Supplementary Fig. 1). The generation of oxygen defects disrupts the inherent symmetry of the crystalline structure. A higher formation energy of oxygen vacancies in CFTS5 indicates that oxygen is difficult to escape from the crystal lattice, concurrently mitigating the perturbations in lattice stresses (Fig. 1d). After entropy modulation, the band center of O 2p orbitals is moved to the depth energy level compared with their counterparts (Fig. 1e), revealing the strengthened TM-O bonding interactions and stabilized crystal structures. For diffusion dynamics, more Na^+ migration pathways are discerned in CFTS5 when viewed parallel to the *ab*-plane, compared to NFM (Fig. 1f). This enhancement is further substantiated by the reduced Na^+ migration energy (Fig. 1g), where CFTS5 has a lower Na^+ migration energy barrier of 1.59 eV in contrast to NFM (1.99 eV). In-depth charge density analysis (Fig. 1h and Supplementary Fig. 2a) reveals that the electrons around oxygen are overall more biased towards the interior of TMO_2 slabs in CFTS5, primarily induced by the presence of Ti and Sn, which reduces electrostatic attraction between the negatively oxygen and the positively sodium, ultimately creating a more conducive environment for Na^+ transport. Moreover, Fig. 1i shows the band gap of NFM is about 1.09 eV, higher than that of CFTS5 (0.71 eV) after Cu, Ti, and Sn co-substitution, implying that it is harder for electrons to be excited from the valence band to the conduction band in NFM, leading to lower intrinsic carrier concentration and conductivity. The pDOS results of different atomic orbits and actual colors of as-obtained layered oxide powders (Supplementary Fig. 2b, c) also provide additional support for this claim.

The structure of as-prepared samples is measured by XRD (Fig. 1b and Supplementary Fig. 3), confirming that all six cathodes show an O3-type $\alpha\text{-NaFeO}_2$ structure with rhombohedral $R\bar{3}m$ space group. Rietveld refinement (Supplementary Tables 2–7) shows that Cu^{2+} , Ti^{4+} , and Sn^{4+} cations are successfully introduced into the TM layers, occupying the octahedral 3b Wyckoff sites. Notably, the co-substitution of Cu, Ti, and Sn atoms results in an initial expansion of *c*-lattice parameter followed by a contraction because of the alteration in the electrostatic interactions with adjacent oxygen layers, induced by the diversity in ionic sizes and electronic properties (Supplementary Fig. 4a). More specifically, the interlayer distance of $d_{(\text{O}-\text{Na}-\text{O})}$ is calculated as 3.23, 3.23, 3.25, 3.28, 3.29, and 3.26 Å for NFM, CFTS3, CFTS4, CFTS5, CFTS6, and CFTS7, respectively. The large O-Na-O interlayer distance of CFTS5 and CFTS6 with high entropy values typically provides favorable diffusion pathways for Na-ions transport. Moreover, the Cu, Ti, and Sn co-substituted samples exhibit irregular plate-shaped particles with a lateral size of 5–10 μm . In contrast, the control NFM displays smaller particles with a diameter of 1–3 μm and a smoother surface. This suggests that the introduction of Cu, Ti, and Sn promotes the growth of single-crystal particles during the calcination process (Fig. 2a and Supplementary Figs. 5–9). High-resolution transmission electron microscope (HRTEM) was employed to examine the structure of CFTS5 (Fig. 2b and Supplementary Figs. 10). The interplanar distance between adjacent lattice fringes in the HRTEM image is 5.26 Å, in good agreement with the *d*-spacing value of the (003) plane calculated through the Bragg formula, which, together with the

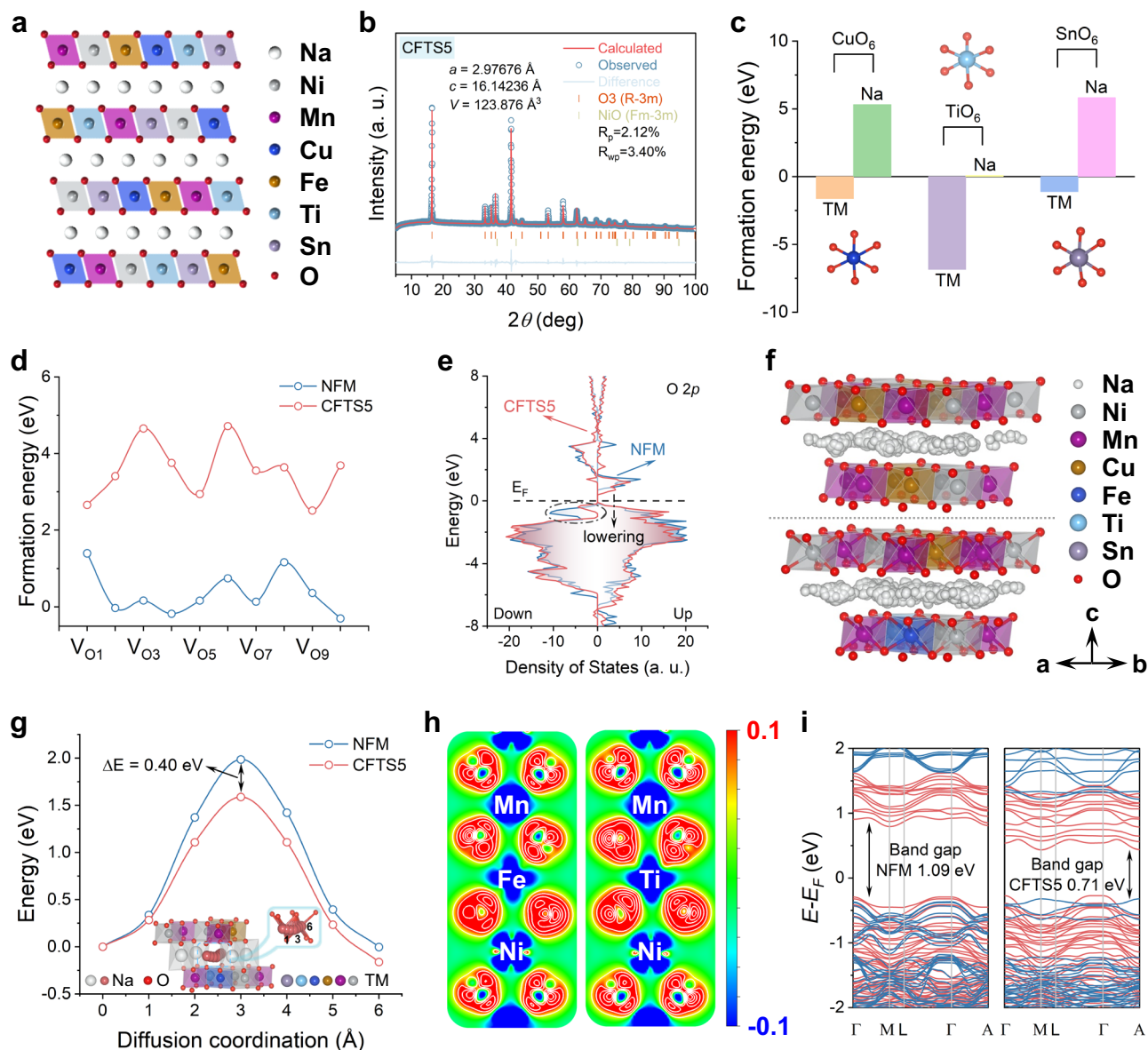


Fig. 1 | Theoretical calculation predictions. **a** Proposed crystal structure. **b** XRD and Rietveld refinement patterns. Theoretical computations of NFM and CFTS5 cathodes: **(c)** formation energy of Cu, Ti, and Sn cations at different sites; **(d)** oxygen-vacancy formation energy; **(e)** O 2p orbit pDOS; **(f)** Na⁺ possible diffusion

pathways in NFM (top) and CFTS5 (bottom); **(g)** Na⁺ diffusion energy barrier of NFM and CFTS5; **(h)** charge density distribution of NFM (left) and CFTS5 (right); **(i)** band structure.

selected area electron diffraction (SAED) images, provides convincing evidence for the layered structure of CFTS5. The energy-dispersive spectroscopy (EDS) mappings show that all elements are uniformly distributed with the slight clustering near the surface (Fig. 2c and Supplementary Figs. 5–9). The time-of-flight secondary ion mass spectrometry (TOF-SIMS) measurement with depth profiles (Fig. 2d and Supplementary Fig. 4b) clearly reveal that the Ni signal is converged in the outer layers and relatively low in the inner layers, and other metal signals are predominantly distributed in the inner layers, with uniform O signal distribution from the top surface to bulk. Moreover, the impact of Cu, Ti, and Sn co-substitution on the valence states of TM cations (Ni, Fe, and Mn) was appraised through XAS and X-ray Photoelectron Spectroscopy (XPS) spectra. Initially, the introduced Cu, Ti, and Sn ions exhibit valence states of +2, +4, and +4, respectively, as examined from the XAS and XPS results (Fig. 2e–h and Supplementary Figs. 11a, b). For CFTS5, a slight shift to low energy is induced in the valence states of Ni²⁺, Fe³⁺, and Mn⁴⁺ with the presence of Cu²⁺, Ti⁴⁺, and Sn⁴⁺. Overall, these results provide evidence that

multicationic zero-Li/Co layered oxide cathodes with six transition-metal cations disordered distribution in TMO₂ slabs have been successfully prepared (Fig. 1a).

Enhanced electrochemical performances with multicationic interactions

The initial galvanostatic charge/discharge (GCD) profiles at 0.1 C (12 mA g⁻¹) in the voltage range of 2.0–4.15 V (Supplementary Fig. 12) show that the specific discharge capacity is recorded as 160.9, 131.1, 131.4, 122.2, 116.9, and 119.2 mAh g⁻¹ for NFM, CFTS3, CFTS4, CFTS5, CFTS6, and CFTS7 with the initial Coulombic efficiency (CE) of 90.7%, 87.8%, 93.9%, 96.8%, 96.7%, and 95.9%, respectively. The difference is that NFM exhibits a short voltage plateau above 4.1 V. The dramatic volumetric strain may be elicited at the high-voltage plateaus, mainly caused by the in-plane TMO₆ distorted and increased repulsion between adjacent TMO₂ slabs upon Na⁺ deep extraction, which is detrimental for the structural stability during long-term cycling. However, the plateau is absent after Cu, Ti, and Sn substitution. To

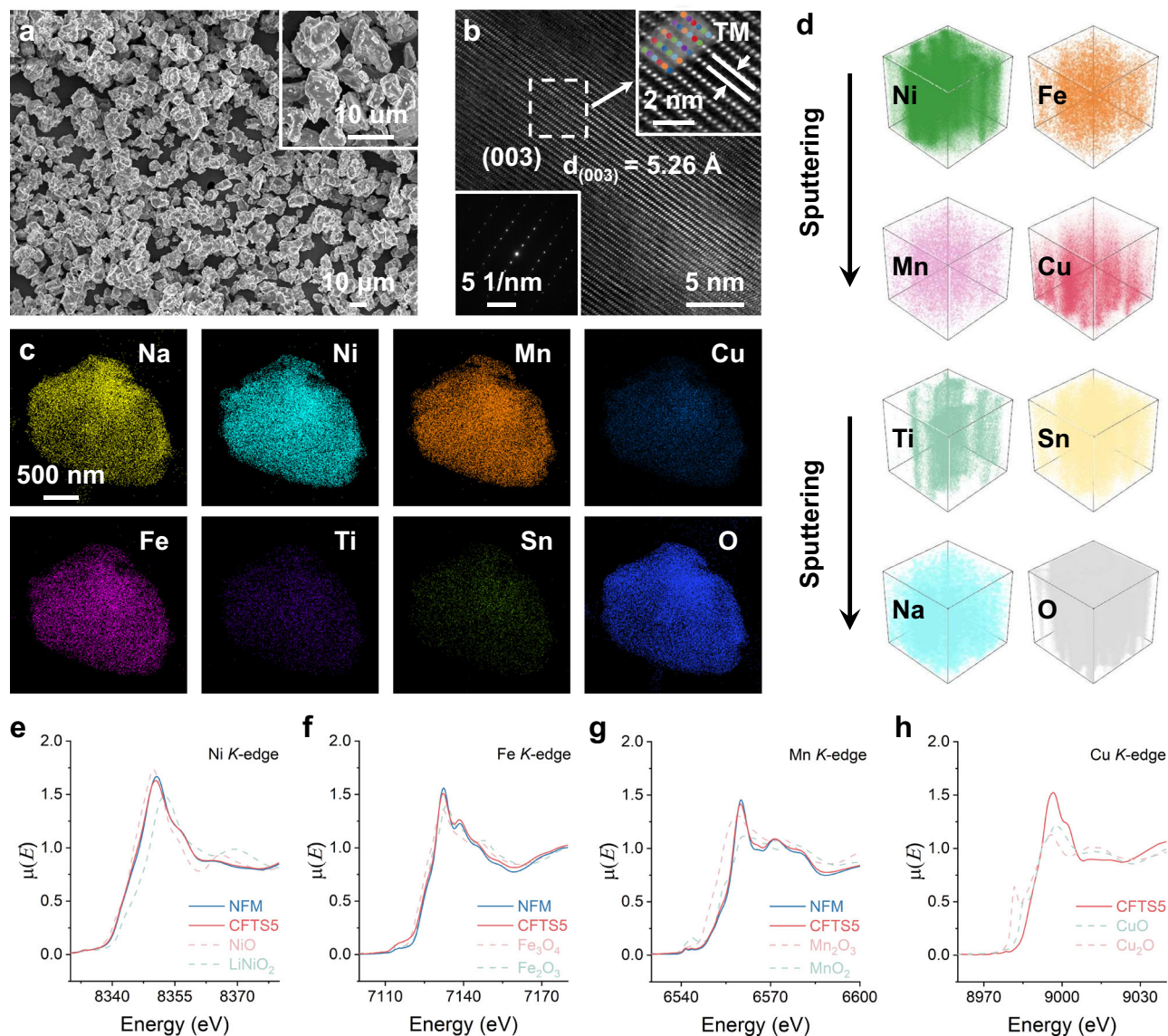


Fig. 2 | Structural characterizations. **a** SEM image. **b** HRTEM and SAED images along the [010] zone axis. **c** EDX elemental mappings of Na, Ni, Mn, Cu, Fe, Ti, Sn, and O of CFTS5 cathodes. **d** TOF-SIMS 3D images of CFTS5 cathodes. XANES spectra at the (e) Ni, (f) Fe, (g) Mn, and (h) Cu K-edges of NFM and CFTS5 cathodes.

further estimate the percentage of O- and P-type phases, the discharge curves of the remaining five compositions were compared and analyzed (Supplementary Fig. 13). The slope in the discharge curve is recognized as the characteristics of the P-type phase and the plateau represents the O-type phase³. From the discharge profiles, the main capacities disparity of all cathodes lies with capacity contribution of the O-type phase. Furthermore, it is noted that even in the case of the same cation co-substitution, the configurational entropy alteration has an impact on the stability of electrochemical properties (Fig. 3a and Supplementary Fig. 14a). Specifically, a cycling durability of only 65.7% capacity retention at 1 C (120 mA g⁻¹) after 100 cycles is achieved for NFM cathodes, albeit with the highest initial capacity of 131.5 mAh g⁻¹. The cycling reliability in CFTS3 cathodes is effectively improved to 80.0% after 100 cycles through the incorporation of Cu, Ti, and Sn cations, while the initial capacity is decreased abruptly to 96.9 mAh g⁻¹. When further adjusting the cation fraction to alter the configurational entropy, capacity retention of 94.8% and 95.8% after 100 cycles is exhibited by CFTS5 and CFTS6 cathodes, compared to 87.5% and 94.2% for CFTS4 and CFTS7 cathodes, respectively, revealing the structural integrity is improved with the entropy increase. The energy density of all species was converted (Fig. 3c), indicating that CFTS5

cathodes have the highest energy density after about 20 cycles. Compared to CFTS5, the slightly reduced capacity and energy density of CFTS6 with the maximum entropy are likely related to the substitution of more reactive cations (Fe³⁺) with inactive cations (Ti⁴⁺ and Sn⁴⁺). Therefore, CFTS5 cathodes with the sub-highest entropy were chosen as the focal point of our experimental investigations. It is involved with a trade-off of sacrificing tiny cyclic stability in exchange for achieving higher capacity and energy density. Long-term cycles at high current densities were also carried out to validate the heightened structural durability of CFTS5 cathodes with multicationic interactions. The comparative cycling behavior of all zero-Li/Co layered oxide cathodes was examined after an initial activation of 3 cycles at 0.1 C (12 mA g⁻¹). After 200 cycles at 2 C (240 mA g⁻¹), CFTS5 samples maintain a high capacity throughout the entire cycle life (Supplementary Fig. 14b). Even after 500 cycles at 5 C (600 mA g⁻¹), a capacity of 83.5% is still retained in CFTS5 cathodes (Fig. 3b). The notable high capacity retention can be traced to the multicationic effect, which is derived from the disordered deployment of transition metals on the same lattice sites, yielding more activated sites, less local strain accumulation, and hence improved intraparticle stability¹². In contrast, the relatively inferior cycling stability of NFM, despite its high initial

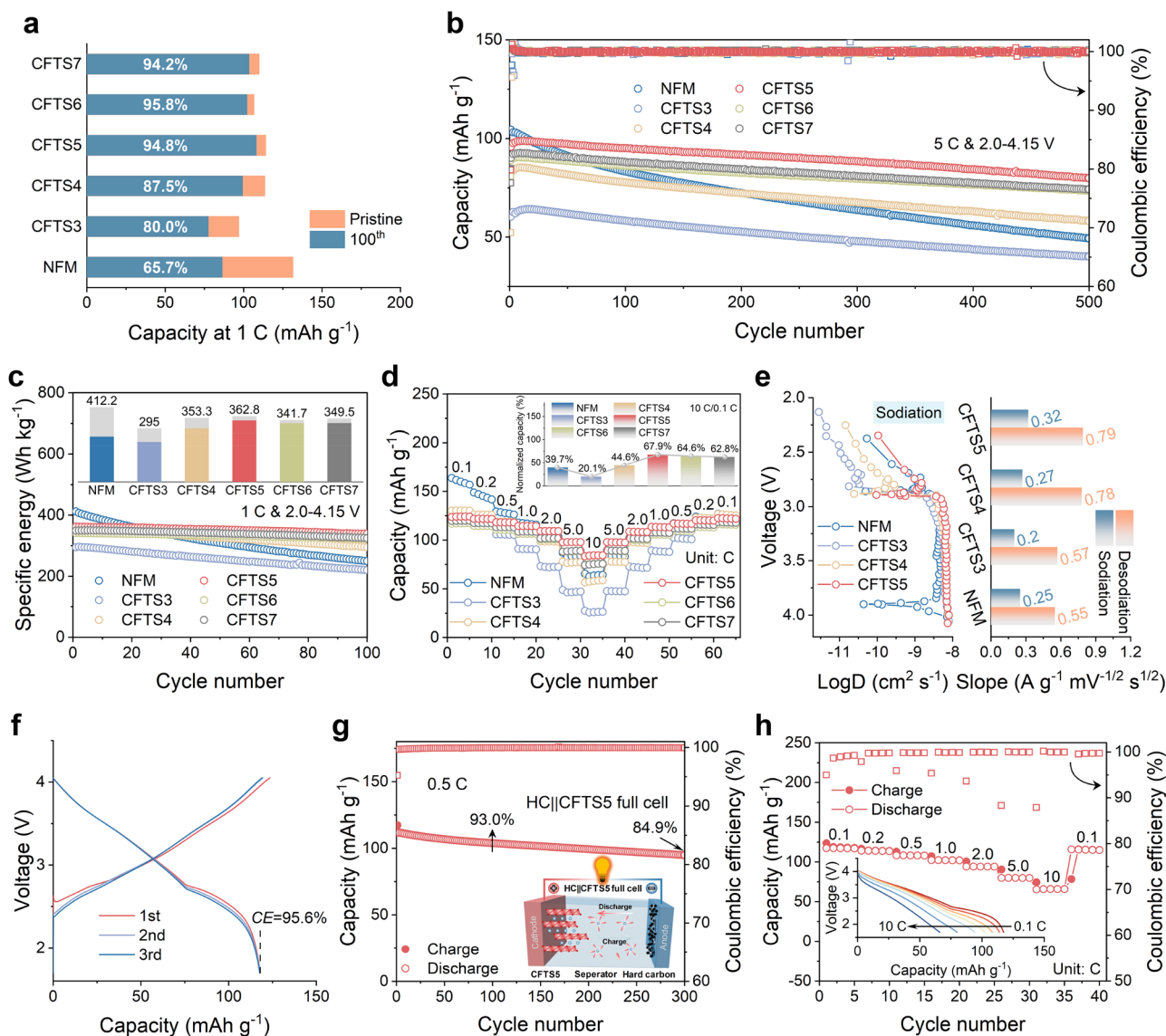


Fig. 3 | Electrochemical performances. **a, c** Cycling stability and the corresponding energy density over 100 cycles at 1 C. **b** Cycling performance over 500 cycles at 5 C. **d** Rate capability. Comparative analysis of Na⁺ diffusion coefficients based on **(e)** GITT tests and rate CV curves. The active mass loading in the half cell is

2–3 mg·cm⁻². **f** Galvanostatic charge-discharge curves, **(g)** cycling performance with N/P ratio of about 1.2, and **(h)** rate capability of Na-ion full cells. The C-rate is defined as 1 C = 120 mA g⁻¹.

discharge capacity, is attributable to the structural destabilization after Na⁺ extraction and volumetric strain-induced intergranular microcracks upon cycling.

To comprehend the (de)intercalation behavior of Na⁺ and the polarization degree of redox pairs, the cyclic voltammetry (CV) curves for the initial cycle were recorded at a sweep rate of 0.1 mV s⁻¹. The primary oxidation/reduction peaks, located at ~3.17/2.83 V, can be attributed to redox couples of Ni²⁺/Ni³⁺ within CFTS5 cathodes. No other redox peak is visible, well consistent with the observations in many O3-type phase layered oxides (Supplementary Fig. 15a)¹³. Yet, an extra pair of redox peaks is exhibited in NFM cathodes, occurring at around 4.15/3.85 V, corresponding to the oxygen redox reaction. This result suggests that the onset of oxygen redox at high voltages is effectively delayed through multicationic interactions, thereby mitigating structural distortions to some extent due to the oxygen loss⁵. Additionally, the minimal polarization potential (0.34 V) between the Ni²⁺/Ni³⁺ redox pairs in CFTS5 stands as the lowest energy barrier for reaction and the swiftest Na⁺ migration among all the zero-Li/Co

layered oxides (Supplementary Fig. 15b). It is noteworthy to mention that the electron delocalization around reactive TM elements can be increased by Ti⁴⁺, owing to the substantial disparity in Fermi levels between Ti⁴⁺ and the reactive cations, begetting the elevation in valence states; parallelly, Sn⁴⁺ with filled d¹⁰ configuration, which abstains from participating in the orbital hybridization within the TMO₂ layer, thereby enhancing the electron density around oxygen and bringing the heightened potentials during the reactive TM redox reaction^{14,15}. However, this underlying principle is not reflected with the escalation of Ti⁴⁺ and Sn⁴⁺ content in the intricate multicationic system relying on the redox peak and average discharge voltage of NFM, CFTS3, CFTS4, CFTS5, CFTS6, and CFTS7 (Supplementary Fig. 15c, d), which reinforces the notion that the “cocktail effect” of high-entropy materials imparts upon them singular and distinctive electrochemical properties. The rate performance was then evaluated by comparing the discharge capacities at current rates ranging from 0.1 C (12 mA g⁻¹) to 10 C (1.2 A g⁻¹) (Fig. 3d). NFM cathodes show a rapid capacity decay during the cycling at 0.1 C (12 mA g⁻¹), which is further exacerbated

with the increased current rates. Conversely, the rate capability is greatly improved in other zero-Li/Co layered oxides, owing to the synergistic effects of Cu, Ti, and Sn. Particularly, CFTS5 and CFTS6 cathodes with a high configurational entropy deliver the enhanced rate capability at 10 C (1.2 A g^{-1}), respectively equal to 67.9% and 64.6% of its reversible capacity at 0.1 C (1.2 A g^{-1}), compared to NFM (39.7%), CFTS3 (20.1%), CFTS4 (44.6%), and CFTS7 (62.8%). The reversible specific capacities of CFTS5 are 124.2, 121.8, 118.2, 114.5, 109.3, 98.0, and 84.3 mAh g^{-1} at current rates of 0.1 (12 mA g^{-1}), 0.2 (24 mA g^{-1}), 0.5 (60 mA g^{-1}), 1.0 (120 mA g^{-1}), 2.0 (240 mA g^{-1}), 5.0 (600 mA g^{-1}), and 10 C (1.2 A g^{-1}), respectively. Moreover, the discharge capacity can be restored back to 122.3 mAh g^{-1} when the current rate decreases to 0.1 C (12 mA g^{-1}), exhibiting excellent capacity recoverability (Supplementary Fig. 16). The galvanostatic intermittent titration technique (GITT) during the second cycle was performed at a rate of 0.1 C (12 mA g^{-1}) (Supplementary Fig. 17a–e). Upon scrutinizing the GITT voltage response profiles within the voltage range of 2.0–4.15 V, the curve of multicationic CFTS5 displays a low overpotential, which is a definitive hallmark of solid-solution behavior. This behavior is responsible for the faster kinetics in comparison to NFM, CFTS3, and CFTS4, agreeing well with the in situ XRD results discussed later. The Na^+ diffusion coefficient (D_{Na^+}), calculated according to the detailed parameters in Methods and Supplementary Table 8, indicates an increased Na-ion mobility in CFTS5, with diffusion coefficients ranging from 9×10^{-11} to $8 \times 10^{-9} \text{ cm}^2 \text{ s}^{-1}$, whereas NFM shows diffusion coefficients in the range of 4×10^{-11} to 5×10^{-9} throughout the charge/discharge process (Fig. 3e and Supplementary Fig. 17f). Furthermore, the CV curve fits and internal/interface impedance results also illustrate the swift Na^+ diffusion kinetics of CFTS5, in good agreement with the GITT results (Fig. 3e and Supplementary Figs. 18, 19). Therefore, the targeted modulation of localized electrons and the improved band structure serve to respectively broaden the pathways for Na^+ transport within alkali metal layers and accelerate electron transfer, together enhancing the rate performance.

To demonstrate the practical utility value of multicationic CFTS5 for SIBs, it is essential to perform comprehensive evaluations of full-cell devices (inset in Fig. 3g). It should be noted that, to offset the full-cell capacity loss due to large Na^+ consumption for the formation of a solid–electrolyte interface (SEI) film on the anode surface, a pre-sodiation strategy was implemented on the HC electrode prior to assembling the full cell (Supplementary Fig. 20). The same trend of CFTS5 cathodes is exhibited in the typical GCD profiles of HC||CFTS5 at 0.1 C (12 mA g^{-1}), with the exception of an overall downward shift in the curve owing to the relatively high potential of HC anode versus Na metals (Fig. 3f). Moreover, a discharge capacity of 118.0 mAh g^{-1} (based on the cathode mass) is attained within the voltage range of 1.7–4.05 V by the full cell, with an initial CE of 95.6%, equating to a specific energy of 258.8 Wh kg^{-1} (based on the cathode and anode mass). A specific capacity of about 111.7 mAh g^{-1} at 0.5 C (60 mA g^{-1}) is delivered by the HC||CFTS5 full cell, maintaining a high capacity retention of 84.9%, even after 300 cycles (Fig. 3g). The rate performances of the full cell, tested from 0.1 C (12 mA g^{-1}) to 10 C (1.2 A g^{-1}) (Fig. 3h), illustrate the delivered discharge capacity remains 65.9 mAh g^{-1} at a high rate of 10 C (1.2 A g^{-1}), corresponding to about 56.2% of its reversible capacity at 0.1 C (12 mA g^{-1}). The inset displays the discharge curves at various rates, unequivocally confirming its excellent high-rate capability. These full-cell configurations are sufficient to affirm that multicationic CFTS5 cathodes hold promise for future industrial applications.

Local coordination stability

The diminution of the local TM–O bond lengths during the desodiation processes, coupled with the decrease of Na content within the lattice structure, results in the built-up of lattice strain, which serves as a trigger for the phase transition¹⁶. In this regard, in situ XRD of the first

two cycles was conducted (Fig. 4a, b and Supplementary Fig. 21). For the multicationic CFTS5, upon the initial Na^+ extraction, the (003) and (006) peaks were shifted towards lower angles, while conversely, the (101), (012) and (104) peaks undergo a precise reversal, which is indicative of the expansion along the *c*-axis coupled with the contraction along the *a*-axis. As further Na^+ is released, a O3–P3 biphasic reaction occurs, followed by a solid-solution reaction of P3 phase up to the charging potential of 4.15 V. A lower O3–P3 structural transition voltage in CFTS5 (3.05 V) compared to NFM (3.14 V) results in a longer P-phase region for CFTS5, which contributes to the improvement of Na^+ transport. Upon the Na^+ reinsertion till around 2.8 V, the P3-type is retained. Then it is turned into a nascent O3' phase, sharing the same rhombohedral structure akin to the pristine O3 structure. With further Na^+ reinsertion, the crystal structure is recovered back to the pristine O3-type phase, corroborated by the ex-situ XRD pattern observed after one cycle (Supplementary Fig. 22a, b). In the following second cycle, multicationic CFTS5 once again undergoes an O3–P3–O3'–O3 evolution, consistent with the first cycle, demonstrating the reversibility of structural transition. However, for NFM, a clear decrease in the intensity of the (003) and (104) peaks upon charging to 4.15 V, indicating the existence of a newly emerged OP2 phase, analogous to the structural transition in $\text{NaNi}_{0.4}\text{Fe}_{0.2}\text{Mn}_{0.2}\text{O}_2$ (Supplementary Fig. 22c)¹⁷. Upon discharge to 2.0 V, a rapid decline in the intensity of the (003) peak of O3 phase suggests a disruption in the long-range structural ordering, leading to the diminished structural reversibility (Supplementary Fig. 22d). The phase transitions of CFTS3, CFTS4, CFTS6, and CFTS7, as reflected by in situ XRD measurements, are similar to those of CFTS5. (Supplementary Figs. 23–26). However, CFTS5 and CFTS6 cathodes, with the sub-highest and highest entropy values, respectively, are shown to exhibit the sub-smallest and smallest angle shifts of the (003) peak among all layered species, further highlighting the positive effect of entropy in mitigating volume variations. Furthermore, the lattice parameters (*a* and *c*) of NFM and CFTS5 cathodes at different charge/discharge states were further extracted from the in situ XRD patterns (Fig. 4c, d). Note that, for multicationic CFTS5, the maximum deviation of *a*-spacing and *c*-spacing during the initial cycle is only 3.0% and 5.5%, respectively, which is lower than that of NFM (3.6% and 6.3%). And upon discharge to 2.0 V, NFM still retains a 2.1% and 1.3% deviation in the *a*-spacing and *c*-spacing, respectively, while there is almost zero for CFTS5. The excellent structural reversibility and minor lattice parameter change of CFTS5 are beneficial from the multicationic interaction effect, which would further decrease the stress accumulation, resulting in suppressing the volume variations and reducing the in-plane disturbances, accounting for the high stability during long-term cycling.

Ex situ XAS spectra were systematically performed at various stages to unravel the alterations in valence states of TM^{n+} and the underlying charge compensation mechanism upon Na^+ (de)intercalation process in multicationic CFTS5. The X-ray absorption near-edge structure (XANES) at the Mn, Ni, and Fe *K*-edges of CFTS5 is depicted in Fig. 4e, g, h, alongside the corresponding Fourier transformed X-ray absorption fine structure (EXAFS) spectra (Fig. 4f, i, j). In the initial charge up to 4.15 V, a subtle chemical shift of Mn *K*-edges is visible during the Na^+ extraction (Fig. 4e). Nonetheless, few Mn ions are engaged in the charge compensation process, since the shape of Mn *K*-edge spectra is sensitive to the local environment of Mn center (Fig. 4f), a phenomenon consistent with previous reports¹⁸. As for the absorption edge of Ni and Fe *K*-edges is right-shifted, suggesting the oxidation of Ni^{2+} and Fe^{3+} to higher valence states, which is demonstrated by the shortened interatomic distances within the first TM–O coordination shell. Concurrently, in the second TM–TM coordination shell, the interatomic distances of Ni and Fe *K*-edges were decreased upon charging, aligning with the contraction of TMO_2 slabs with reduced parameters (Fig. 4g–j). However, lower changes of Ni–O coordination distances in CFTS5

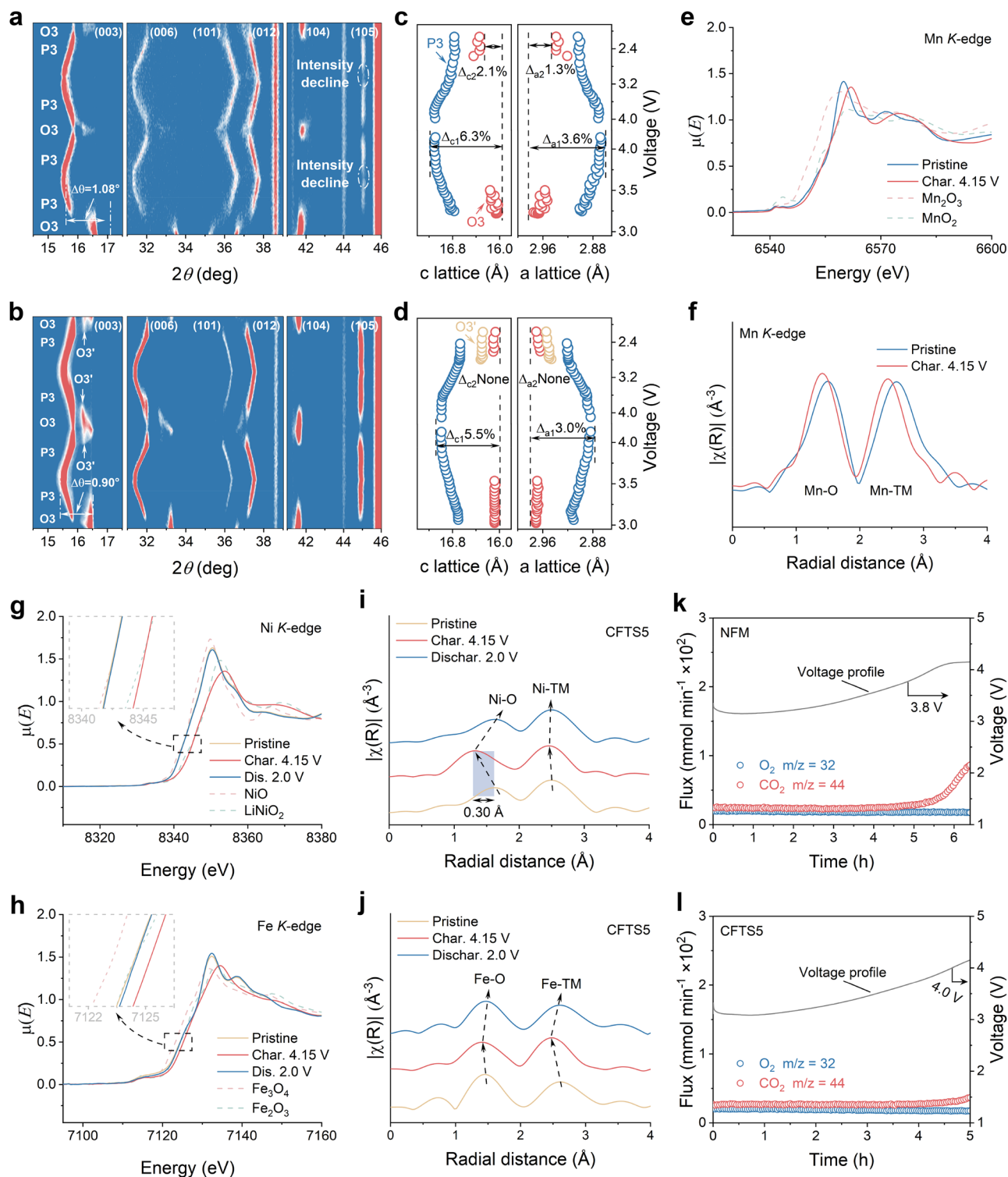


Fig. 4 | Structure and oxygen evolution. Contour plots of in situ XRD patterns and the corresponding crystal parameters evolution of (a, c) NFM, and (b, d) CFTS5 cathodes. Charge compensation mechanism in CFTS5 cathodes. Ex-situ XANES

spectra and the corresponding EXAFS spectra at the (e, f) Mn, (g, i) Ni, and (h, j) Fe K-edges of CFTS5 at different charge/discharge states. DEMS data during the initial cycle of (k) NFM and (l) CFTS5 cathodes (active mass loading of -10 mg cm^{-2}).

(0.30 Å) attest to milder structural stresses relative to NFM (0.34 Å) (Fig. 4i and Supplementary Fig. 29c). Upon discharge to 2.0 V, Ni and Fe K-edges are nearly fully restored back to that of the pristine. The Ni and Fe K-edges in NFM follow a similar behavior (Supplementary Fig. 29). However, when charged to 4.15 V, a notable distinction arises, where Ni in NFM is oxidized to a higher valence state, from $Ni^{2.05+}$ to $Ni^{3.27+}$, in contrast to CFTS5, from $Ni^{2.0+}$ to $Ni^{3.08+}$. Conversely,

a lesser degree of charge transfer is exhibited in NFM with regard to Fe, from $Fe^{3.11+}$ to $Fe^{3.24+}$, as opposed to CFTS5 from $Fe^{3.0+}$ to $Fe^{3.24+}$, which are quantified utilizing the half-height method according to the half-edge energy at the Ni and Fe K-edges (Supplementary Figs. 27–29)¹⁹. These differences suggest that the continued oxidation of Ni is impeded, and the charge compensation of Fe is facilitated through the entropy strategy. The complementarity inherent in

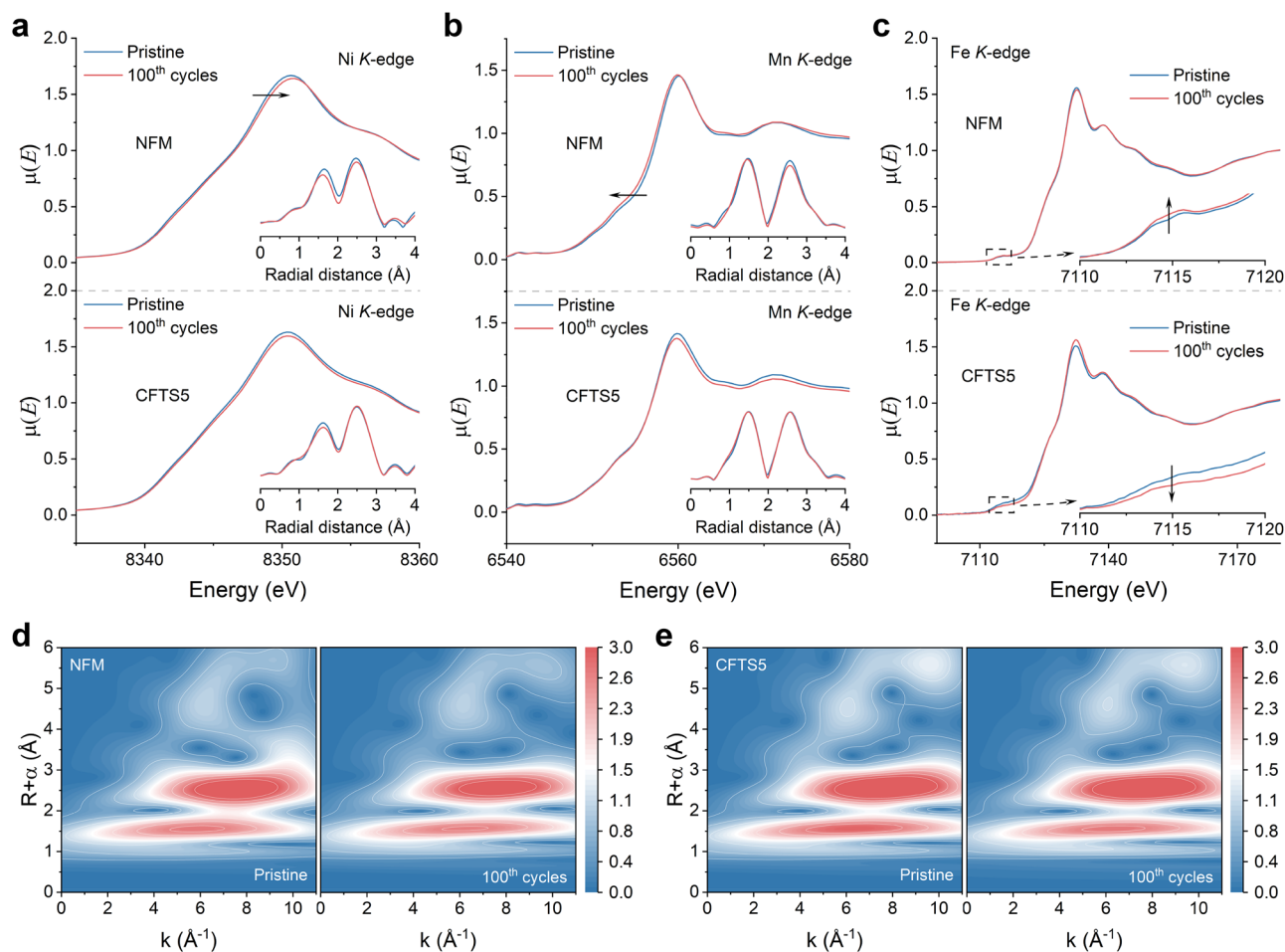


Fig. 5 | Highly stable local coordination environment. Ex-situ XANES spectra and the corresponding EXAFS spectra of cycled NFM and CFTS5 cathodes at (a) Ni, (b) Mn, and (c) Fe K-edges. Contour plots of the Ni K-edge WT-EXAFS spectra for (d) NFM and (e) CFTS5 at the pristine and after cycles.

charge compensation within CFTS5 manifests as an outcome of a myriad of synergistic effects among various TM cations. It is noteworthy that the absorption edge of Cu K-edges is also right-shifted towards higher energy levels, indicating Cu^{2+} also participates in redox to compensate for some capacity lost by reactive Fe dilution (Supplementary Fig. 30). Structural degradation is ordinarily associated with the intricate dynamics of lattice oxygen¹⁸. To further check the oxygen evolution in response to the applied voltage, differential electrochemical mass spectrometry (DEMS) was also implemented to monitor the initial Na^+ (de)intercalation process (Fig. 4k, l). It is worth noting that the lattice oxygen loss of cathode, assisting in the oxidation of the electrolyte, culminates in the emission of CO_2 as a resultant byproduct^{20,21}. Evidently, the formation of CO_2 is postponed for CFTS5 in comparison to NFM, illustrating the multicationic stabilization effect in the crystal structure effectively mitigates adverse side reactions and surficial oxygen defects.

Furthermore, to substantiate the multicationic interactions on the local coordination environments, XAS spectra of CFTS5 and NFM after 100 cycles were captured (Fig. 5a–c). XANES reveals that the Ni and Mn K-edges of cycled CFTS5 is nearly overlapped with those of the pristine sample; by contrast, the Ni K-edge in cycled NFM is shifted towards higher energy and the Mn K-edge in cycled NFM is moved towards lower energy, suggesting some of the interior volumes and residual stresses within NFM cannot be fully reduced (Fig. 5a, b). EXAFS shows negligible shifts and intensity reduction of both TM–O and TM–TM interatomic peaks in cycled CFTS5, reflecting stable local coordination environments during long-term cycles. Furthermore, alterations in the distortions of the Fe coordination structure may lead to the evolution

of pre-edge peak. The enhanced intensity of the pre-edge peak at the Fe K-edges in cycled NFM shows an increased lattice distortion (Fig. 5c), resulting in irreversible migration of Fe ions, while the distortion in CFTS5 is diminished, indicative of the alleviation of localized strains²². To further unveil the local structural stability of multicationic CFTS5, the contour plots of Ni K-edge wavelet-transformed (WT) EXAFS spectra were generated (Fig. 5d, e). Two distinct scattering peaks located at around $(6.3 \text{ \AA}^{-1}, 1.6 \text{ \AA})$ and $(7.7 \text{ \AA}^{-1}, 2.6 \text{ \AA})$ can be assigned to the features of Ni–O and Ni–TM coordination shells, respectively. In case of the NFM, the Ni–O and Ni–TM features exhibit a dramatical alteration in shape after long-term cycling, indicating lattice shrinkage and generation of defects. In contrast, a negligible change in the Ni–O and Ni–TM features is exhibited in the multicationic CFTS5, confirming multicationic interactions contribute to the establishment of a highly stable local coordination environment within the crystal structure, thereby reducing overall anisotropic lattice strain.

Thermal stability and postmortem analysis

Directly, the atomic-scale structure evolution was captured by means of STEM-HAADF/ABF and the corresponding fast Fourier transform (FFT) patterns to unravel extraordinary structural stability derived from multicationic effect (Fig. 6a, b and Supplementary Fig. 31). After 100 cycles, the surface layered structure (region II) in NFM is clearly disrupted by the severe Na^+/TM intermixing rock-salt structure ($Fd-3m$) (region I), epitaxially growing on the particle edges along the (003) plane, up to ~10 nm in length. Additionally, a serious cationic irreversible migration from TMO_2 slabs to NaO_2 slabs is also observed

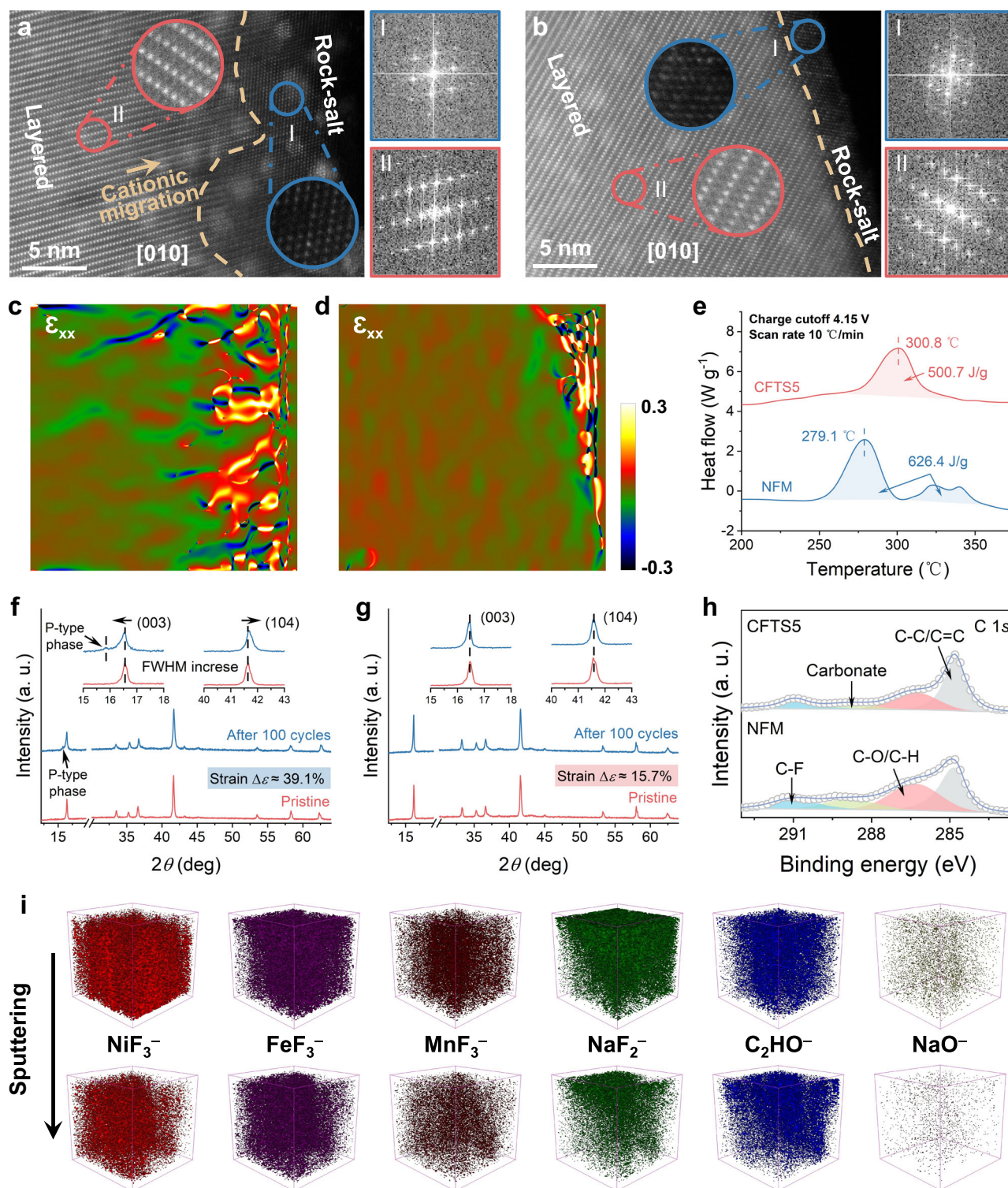


Fig. 6 | Morphological and microstructural evolution and thermal stability. HAADF-STEM and the corresponding FFT images of (a) NFM and (b) CFTS5 cathodes after 100 cycles. Strain state of cycled (c) NFM and (d) CFTS5 obtained by

geometrical phase analysis (GPA). **e** Ex-situ DSC profile. Ex-situ XRD patterns of (f) NFM and (g) CFTS5 cathodes. **h** XPS spectra of C 1s. (i) TOF-SIMS 3D images of cycled electrodes.

in the near-surface region in NFM. Contrastingly, for multicationic CFTS5, a faint trace of the rock-salt phase, spanning only ~3 nm near the surface, is detected, and cationic irreversible migration is almost absent. The cross-sectional SEM analysis, along with the corresponding EDS line profiles, is further performed to confirm the stabilizing effect of entropy on the near-surface structure (Supplementary Fig. 32). Strain analyzes (Fig. 6c, d) of the cycled particles reveal that

CFTS5 remains minimal defects and strain primarily concentrated on the surface, but nearly free in bulk; by contrast, NFM shows the formation of extensive dislocations extending from the interior outward. Furthermore, several microcracks, derived from strong stress cumulations, are observed in NFM particles, whereas no cracks for CFTS5 particles, maintaining a robust single-crystal morphology as shown by SEM images (Supplementary Fig. 33). These apparent differences in

structural integrity serve as concrete evidence affirming the alleviated internal strain within CFTSS. To evaluate the impact of the entropy regulation strategy on the thermal runaway behavior, DSC tests were performed on NFM and CFTSS cathodes after charging to 4.15 V (soaking in fresh electrolyte) (Fig. 6e)²³. The exothermic peak located at 279.1 °C in the case of NFM is closely associated with the electrolyte oxidation and decomposition on the surface of the active cathode materials, yet the triggering temperature is clearly delayed for CFTSS cathodes (300.8 °C). The enthalpy quantification related to the exothermic peaks of CFTSS cathodes is 500.7 J g⁻¹, much lower than that of NFM cathodes (626.4 J g⁻¹). These results provide compelling confirmation of the substantial enhancement in thermal stability achieved through the implementation of the rational entropy regulation. To demonstrate the cycling robustness, the structures of pristine and post-cycling electrodes were carefully compared through ex-situ XRD measurements (Fig. 6f, g). Notably, NFM undergoes a pernicious transformation in structural configuration, changing from O-type phase to P-type phase after 100 cycles, as substantiated by the appearance of a diffraction peak at $2\theta \approx 15.8^\circ$. Moreover, a deviation is discerned in the (003) peak of the O3 phase, shifting towards a lower angle, while the converse alteration is noted in the (104) peak, suggesting an expansion along the *c*-axis and a simultaneous contraction along the *a*-axis. Severe strain accumulation ($\approx 39.1\%$) is further mirrored by the increase of the full width at half maximum (FWHM) of the peaks within the cycled NFM particles based on a typical Williamson–Hall analysis (Methods and Supplementary Table 9, 10). Comparatively, untraceable shifts and minimal strain accumulation ($\approx 15.7\%$) are exhibited in the diffraction patterns of CFTSS, even after 100 cycles, attesting to the enduring structural configuration attributed to the multicationic stabilization mechanisms. The multicationic interactions on the cathode-electrolyte interface (CEI) formation was examined through a comparative analysis of XPS spectra for post-cycling electrodes (Fig. 6h). The C 1s spectrum is deconvoluted into four distinct peaks: one at 284.8 eV, representing C–C/C=C moieties within the conductive carbon matrix; another at 286.3 eV, indicative of C–O/C–H functional groups; a third at 288.7 eV, denoting the presence of carbonate species; and a fourth at 290.9 eV, corresponding to C–F derived from the PVDF binder on the cathode surface^{4,24}. A careful comparative assessment of the XPS spectra unveils that upon the rational introduction of Cu, Ti, and Sn, a noticeable reduction occurs in the area of C–O/C–H and carbonate species under the curve, which is associated with the electrolyte decomposition. The diminished area pertaining to C–O/C–H and carbonate peaks points towards the suppression of both interfacial parasitic reactions and electrolyte degradation at the cathode surface when multiple cations are integrated into the lattice structure, ultimately yielding a reduced CEI thickness. Intuitively, time-of-flight secondary-ion mass spectrometry (TOF-SIMS) analysis on the cycled cathodes was performed to visualize chemical evolution at the electrolyte-cathode interphase (Fig. 6i)^{25,26}. More discernible signals are detected in NFM, including metal fluorinated species (specifically, NiF_3^- , FeF_3^- , MnF_3^- and NaF_2^-) formed as the reaction byproducts arising from the interplay of metal ions with hydrofluoric acid (HF), the electrolyte component (C_2HO^-), as well as the residual sodium species (NaO^-) left upon the cathode surface²⁵. The formation of the aforementioned metal fluorides not only catalyzes the cathode surface erosion and irreversible electroactive TM ions loss but also poses an impediment to the efficient Na^+ transport across the thick CEI, ultimately leading to a serious deterioration in electrochemical performance.

Discussion

In summary, we demonstrate a strain-depressant strategy via introducing multicationic interactions into a zero-lithium/cobalt layered oxide cathode to alleviate the persistent accumulation of lattice strain during sodium (de)intercalation. Owing to the chemical compatibility,

these alio-/iso-valent cations are disorderly deployed in the octahedral sites of TMO_2 slabs. The oxygen stability and volumetric vibrations of the cathode during operation are improved in response to such multicationic structure, thereby preventing near-surface structure deconstruction, interface side reactions, and microcrack formation. Aided by the complex lattice system, the phase transition of $\text{O3-P3-O3}'$ -O3 evolution in the multicationic cathode exhibits great reversibility, and the local octahedral coordination environment remains highly stable even after 100 cycles within the voltage of 2.0–4.15 V. Furthermore, the targeted modulation of localized electrons, coupled with the large O–Na–O interlayer spacing through the rational entropy regulation, serves to diminish the Na–O bonding energy, broaden the pathways for Na^+ transport within NaO_2 slabs. Consequently, the multicationic cathode displays an excellent cycling performance, giving an improved 94.8% capacity retention over 100 cycles at 1 C (120 mA g⁻¹) and 83.5% capacity retention over 500 cycles at 5 C (600 mA g⁻¹), and high-rate capability, delivering 124.2 mAh g⁻¹ at 0.1 C (12 mA g⁻¹) and 84.3 mAh g⁻¹ at 10 C (1.2 A g⁻¹). The full-cells deliver a discharge capacity of 118.0 mAh g⁻¹, maintaining an 84.9% capacity retention over 300 cycles at 0.5 C (60 mA g⁻¹). The feasible entropy regulation approach advances the outlook for commercial viability of safe, low-cost, and long-life sodium-ion battery cathodes.

Methods

Materials synthesis

A series of Li-/Co-free, multicationic O3-structured layered oxides with the composition $\text{NaNi}_{0.35}\text{Mn}_{0.35}\text{Cu}_{2x}\text{Fe}_{0.3-4x}\text{Ti}_x\text{Sn}_x\text{O}_2$ ($x = 0, 0.03, 0.04, 0.05, 0.06$, and 0.07) were synthesized using a solid-state method. In a typical synthesis, precise stoichiometric amounts of Na_2CO_3 (Macklin, >99.9%, with a 5% excess of sodium), NiO (Aladdin, >99.0%), MnO_2 (Aladdin, >99.0%), CuO (Aladdin, 99.9%), Fe_2O_3 (Macklin, >99.9%), TiO_2 (Macklin, >99.8%), and SnO_2 (Macklin, >99.5%) were mixed through ball-milling for 12 h, utilizing isopropanol (Sinopharm, >99.7%) as a dispersant at a rotation rate of 400 revolutions per minute. After drying at 60 °C for 6 h, the resultant mixture was pressed into pellets under a pressure of 10 MPa, followed by calcination for 15 h at 1000 °C in an air atmosphere with a ramping rate of 3 °C per minute. The final products were allowed to cool naturally to -150 °C and then transferred into an argon-filled glove box to prevent exposure to the air.

Materials characterization

SEM images were collected on a field emission scanning electron microscopy (FESEM, TESCAN MIRA3 LMU). XRD patterns were recorded on a Rigaku Ultima IV x-ray diffractometer with $\text{Cu K}\alpha$ radiation ($\lambda = 1.54059 \text{ \AA}$). The average chemical compositions were determined by an inductively coupled plasma optical emission spectrometer (ICP-OES). TEM images were collected on a Titan G2 60–300 (USA) with an energy dispersive X-ray spectroscopy (EDS). A transmission electron microscope (TEM, Talos F200x, America) with energy dispersive X-ray spectroscopy (EDS) and a FEI Titan Cubed G2 60–300 aberration-corrected scanning transmission electron microscope (STEM) at 200 kV were used to investigate the detailed microstructure. A specially designed cell model equipped with a Be window for X-ray penetration for in situ XRD experiments at 0.2 °C (24 mA g⁻¹) during the charge and discharge process. Time-of-flight secondary ion mass spectrometry (TOF-SIMS, PHI NanoTOFII) was employed for the characterization of surficial chemical species. The QAS100 Li instrument coupled with a SWAGELOK-type cell (60 μL electrolyte, active mass loading of $\sim 10 \text{ mg cm}^{-2}$, and Whatman GF/D glass fiber as the separator) was used to collect the differential electrochemical mass spectrometry (DEMS) spectra with Ar as the carrier gas at a flow rate of 1 mL min^{-1} . For all ex-situ characterizations, the cycled electrode samples in target states were disassembled, rinsed with DMC, dried, and sealed in the argon-filled glove box at $25 \text{ }^\circ\text{C} \pm 2 \text{ }^\circ\text{C}$.

X-ray absorption spectroscopy

XAFS spectra at the Ni, Mn, Cu, and Fe *K*-edge were recorded at the BL11B beamline of Shanghai Synchrotron Radiation Facility (SSRF). The incident photons were monochromatized by a Si(111) double-crystal monochromator. The energy calibration was performed using a Ni, Mn, Cu, and Fe reference foil. All the spectra were measured in both transmission and fluorescence modes using a home-made ionization chamber filled with Ar.

Configuration entropy S_{conf}

Configuration entropy S_{conf} of the as-prepared cathode materials was calculated based on the equation:

$$S_{\text{conf}} = -R \left\{ \left(\sum_{i=1}^N x_i \ln x_i \right)_{\text{cation-site}} + \left(\sum_{j=1}^M x_j \ln x_j \right)_{\text{anion-site}} \right\}$$

where x_i and x_j represent the mole fraction for each element, and R is the gas constant.

Galvanostatic intermittent titration technique

Na^+ diffusion coefficients were calculated from the Galvanostatic intermittent titration technique results based on the equation:

$$D_{\text{Na}^+} = \frac{4}{\pi\tau} \left(\frac{m_B V_m}{M_B S} \right)^2 \left(\frac{\Delta E_s}{\Delta E_\tau} \right)^2 \left(\tau \ll L^2/D \right)$$

where τ denotes the duration of a constant current pulse (s), m_B represents the mass of the active materials (g), V_m stands for the molar volume of a single unit cell ($\text{cm}^3 \text{mol}^{-1}$), M_B signifies the molecular weight of the obtained cathode materials (g mol^{-1}), S represents the surface area of the electrolyte/electrode interface (cm^2), ΔE_s represents the steady-state voltage variation at rest, ΔE_τ accounts for the total voltage differential during a constant current pulse, and L signifies the diffusion distance for Na^+ ions from the lattice to the electrolyte.

Williamson–Hall analysis

A typical Williamson–Hall analysis was conducted to gain more insights of lattice strain. This analysis shows that the broadening of XRD diffraction peaks in the sample is caused by both crystallite size and microstrain, which have different dependencies on the Bragg angle (θ). These contributions can be quantified using the following equation:

$$\beta_{\text{total}} = \beta_{\text{size}} + \beta_{\text{strain}} = \frac{K\lambda}{L \cos \theta} + 4\varepsilon \frac{\sin \theta}{\cos \theta}$$

Where β_{size} , β_{strain} , and β_{total} refer to the crystallite size, strain, and total broadening, respectively. K is a constant dependent on crystallite shape, λ is the X-ray wavelength, L represents the crystallite size, and ε is the lattice microstrain. For simplicity, we assume that both size and strain contribute equally to the overall peak broadening.

DFT calculations

First-principles calculations were conducted employing the Vienna ab initio simulation program (VASP)²⁷, grounded in the density-functional theory (DFT) framework and the projector augmented-wave (PAW) method²⁸. The exchange correlation effects were modeled by generalized gradient approximation (GGA) method of Perdew–Burke–Ernzerhof (PBE) introduced into function²⁹. The Hubbard-type correction U_{eff} ($U_{\text{eff}} = U - J$) for the 3d-orbitals in Ni, Mn, Cu, Fe, and Ti ions was established as 5.3, 3.9, 4.0, 4.9, and 2.4 eV, respectively³⁰. The plane-wave energy cutoff was set at 500 eV, and convergence was adjudged achieved when the Hellmann–Feynman forces acting upon

each atom were constrained to be under $0.01 \text{ eV } \text{\AA}^{-1}$. Simultaneously, the total energy convergence was rigorously maintained at up to 10^{-5} eV . The gamma-centered Monkhorst-Pack K-point mesh was applied to grids of $5 \times 3 \times 1$ for the optimization of structure in the $1 \times 2 \times 1$ supercells of NFM and CFTSS cathodes. The deformation charge density was calculated by subtracting atomic charge density from total charge density. The density of both spin-up and spin-down states was included in the projected DOS. The crystal orbital Hamilton Populations were calculated by using LOBSTER code.

Electrochemical measurements

Each working cathode was crafted through amalgamating 80 wt.% active materials (480 mg) with 10 wt.% super P (60 mg) and 10 wt.% polyvinylidene fluoride (PVDF, 60 mg) in N-methylpyrrolidone (NMP, Sinopharm, >99%) solvent. This slurry was ball milled at $25 \text{ }^\circ\text{C} \pm 2 \text{ }^\circ\text{C}$ in air and artfully laid upon a carbon-coated aluminum foil using an automatic coating machine and dried at $120 \text{ }^\circ\text{C}$ for 10 h within a vacuum. The electrodes were cut into disks (14 mm in diameter) using MSK-T10 Manual Slicer (Shenzhen Kejing Star Technology Co., Ltd) with the active material loading of $2\text{--}3 \text{ mg cm}^{-2}$ without the calendaring procedure. The assembly of CR2016 coin-type cells took place within an argon-filled glove box, where H_2O and O_2 were strictly maintained below 0.01 ppm. The configuration featured a Na metal (Aladdin, >99.7%, $16 \text{ mm} \times 0.5 \text{ mm}$, diameter \times thickness)/hard carbon (Kuraray China Co., Ltd) as counter/reference electrode, a glass fiber membrane (Whatman, GF/D, 19 mm in diameter) as separator, and about 50 μL electrolyte (Duoduo Chemical Technology Co., Ltd) consisting of 1 M NaClO_4 in propylene carbonate (PC, 100 vol%) with 5.0 % fluorinated ethylene carbonates (FEC). GCD measurements were executed using a NEWARE Battery test System (CT-4008T-5V50Ma-164, Shenzhen, China) in voltage ranges of 2.0–4.15 V. GITT was employed within the potential window of 2.0–4.15 V by recurring current pulses for 15 min at 0.1 C (12 mA g^{-1}) followed by a 3 h rest. CV and EIS were recorded by an Autolab electrochemical workstation (MULTI AUTOLAB M204). For each electrochemical measurement, three independent cells were evaluated at least. The data reported herein are derived from a representative cell exhibiting median performance, selected to reflect its typical electrochemical behaviors. Hard carbon anodes were made via blending the active materials (90 wt.%, 360 mg), Super P (5 wt.%, 20 mg), and PVDF (5 wt.%, 20 mg) within a NMP solvent. The resultant slurry was cast upon a carbon-coated aluminum foil for full cells. Regarding full cells (HC||CFTSS), cathode/anode electrodes were balanced with negative/positive (N/P) ratio of around 1.2 referenced to the capacity in half cells. After that, the anode electrodes were loaded into half-cells for 10 cycles within the voltage range of 0.01–3.0 V, terminating at 0.2 V in the discharged state to form the stable SEI film and prevent irreversible capacity loss in the full cell due to SEI formation. The electrochemical performance of full cells was evaluated in the voltage range of 1.7–4.05 V. All electrochemical tests were performed at $25 \text{ }^\circ\text{C} \pm 2 \text{ }^\circ\text{C}$ in air unless otherwise specified.

Data availability

All relevant data supporting our study are provided in the manuscript and Supplementary Information file. Source data are available from the corresponding author upon request. Source data are provided with this paper.

References

- Wang, L., Liu, T., Wu, T. & Lu, J. Strain-retardant coherent perovskite phase stabilized Ni-rich cathode. *Nature* **611**, 61–67 (2022).
- Chen, Y. et al. Opportunities for high-entropy materials in rechargeable batteries. *ACS Mater. Lett.* **3**, 160–170 (2020).
- Zhao, C., Ding, F., Lu, Y., Chen, L. & Hu, Y. S. High-entropy layered oxide cathodes for sodium-ion batteries. *Angew. Chem. Int Ed.* **59**, 264–269 (2020).

4. Joshi, A. et al. High-entropy co-free O3-type Layered oxyfluoride: a promising air-stable cathode for sodium-ion batteries. *Adv. Mater.* **35**, 2304440 (2023).
5. Yao, L. et al. High-entropy and superstructure-stabilized layered oxide cathodes for sodium-ion batteries. *Adv. Energy Mater.* **12**, 2201989 (2022).
6. Yang, L. et al. Lithium-doping stabilized high-performance $\text{P2-Na}_{0.66}\text{Li}_{0.18}\text{Fe}_{0.12}\text{Mn}_{0.7}\text{O}_2$ cathode for sodium ion batteries. *J. Am. Chem. Soc.* **141**, 6680–6689 (2019).
7. Manthiram, A. A reflection on lithium-ion battery cathode chemistry. *Nat. Commun.* **11**, 1550 (2020).
8. Wang, H. et al. Large-scale synthesis of $\text{NaNi}_{1/3}\text{Fe}_{1/3}\text{Mn}_{1/3}\text{O}_2$ as high performance cathode materials for sodium ion batteries. *J. Electrochem. Soc.* **163**, A565 (2016).
9. Xu, L. et al. Engineering functionalized 2D metal-organic frameworks nanosheets with fast Li^+ conduction for advanced solid li batteries. *Adv. Mater.* **35**, 2303193 (2023).
10. Chu, S., Guo, S. & Zhou, H. Advanced cobalt-free cathode materials for sodium-ion batteries. *Chem. Soc. Rev.* **50**, 13189–13235 (2021).
11. Miracle, D. B. & Senkov, O. N. A critical review of high entropy alloys and related concepts. *Acta Mater.* **122**, 448–511 (2017).
12. Wang, H. et al. High-entropy Na-deficient layered oxides for sodium-ion batteries. *ACS Nano* **17**, 12530–12543 (2023).
13. Hong, N. et al. An in situ dual-modification strategy for O3- $\text{NaNi}_{1/3}\text{Fe}_{1/3}\text{Mn}_{1/3}\text{O}_2$ towards high-performance sodium-ion batteries. *J. Mater. Chem. A* **11**, 18872–18880 (2023).
14. Yao, H.-R. et al. Designing air-stable O3-type cathode materials by combined structure modulation for Na-ion batteries. *J. Am. Chem. Soc.* **139**, 8440–8443 (2017).
15. Wang, P. F. et al. An abnormal 3.7 Volt O3-type sodium-ion battery cathode. *Angew. Chem. Int. Ed.* **57**, 8178–8183 (2018).
16. Huang, W. et al. Unrecoverable lattice rotation governs structural degradation of single-crystalline cathodes. *Science* **384**, 912–919 (2024).
17. Yuan, D. D., Wang, Y. X., Cao, Y. L., Ai, X. P. & Yang, H. X. Improved electrochemical performance of Fe-substituted $\text{NaNi}_{0.5}\text{Mn}_{0.5}\text{O}_2$ cathode materials for sodium-ion batteries. *ACS Appl. Mater. Interfaces* **7**, 8585–8591 (2015).
18. Guo, Y.-J. et al. Boron-doped sodium layered oxide for reversible oxygen redox reaction in Na-ion battery cathodes. *Nat. Commun.* **12**, 5267 (2021).
19. Ren, M. et al. Homeostatic solid solution in layered transition-metal oxide cathodes of sodium-ion batteries. *J. Am. Chem. Soc.* **145**, 224–233 (2022).
20. Qin, Z. et al. A universal molten salt method for direct upcycling of spent Ni-rich cathode towards single-crystalline Li-rich cathode. *Angew. Chem.* **62**, e202218672 (2023).
21. Wang, H. et al. Halting oxygen evolution to achieve long cycle life in sodium layered cathodes. *Angew. Chem. Int. Ed.* **64**, e202418605 (2024).
22. Gao, X. et al. Origin of fast capacity decay in Fe-Mn-based sodium layered oxides. *Adv. Funct. Mater.* **33**, 2212685 (2023).
23. Xie, Y. et al. Probing thermal and chemical stability of $\text{NaNi}_{1/3}\text{Fe}_{1/3}\text{Mn}_{1/3}\text{O}_2$ cathode material toward safe sodium-ion batteries. *Chem. Mater.* **30**, 4909–4918 (2018).
24. Jiang, M. et al. Enabling the Nb/Ti co-doping strategy for improving structure stability and rate capability of Ni-rich cathode. *Chin. Chem. Lett.* **36**, 110040 (2024).
25. You, Y. et al. Insights into the improved high-voltage performance of Li-incorporated layered oxide cathodes for sodium-ion batteries. *Chem* **4**, 2124–2139 (2018).
26. Zou, K. et al. Thermodynamics-directed bulk/grain-boundary engineering for superior electrochemical durability of Ni-rich cathode. *J. Energy Chem.* **97**, 321–331 (2024).
27. Kresse, G. & Hafner, J. Ab initio molecular dynamics for liquid metals. *Phys. Rev. B* **47**, 558 (1993).
28. Blöchl, P. E., Jepsen, O. & Andersen, O. K. Improved tetrahedron method for Brillouin-zone integrations. *Phys. Rev. B* **49**, 16223 (1994).
29. Perdew, J. P., Burke, K. & Ernzerhof, M. Generalized gradient approximation made simple. *Phys. Rev. Lett.* **77**, 3865 (1996).
30. Wang, L., Maxisch, T. & Ceder, G. Oxidation energies of transition metal oxides within the GGA+U framework. *Phys. Rev. B* **73**, 195107 (2006).

Acknowledgements

This work was financially supported by the National Natural Science Foundation of China (52325405 [X.J.], U21A20284 [X.J.], 52261135632 [X.J.]) and Postgraduate Innovation Program of Hunan Province (CX20240205 [H.W.]). We are grateful for the support from the High-Performance Computing Center of Central South University in theoretical calculations and Shiyanjia Lab (www.shiyanjia.com) in characterizations. The XAFS measurements were performed at BL11B beamline of Shanghai Synchrotron Radiation Facility (SSRF) and the BL12B-a&b station in the National Synchrotron Radiation Laboratory (NSRL) for XAS. We also acknowledge support from the US Department of Energy (DOE), Office of Energy Efficiency and Renewable Energy (EERE), Vehicle Technologies Office (VTO). This work was also supported by Clean Vehicles, US–China Clean Energy Research Centre (CERC-CVC2) under the US DOE EERE Vehicle Technologies Office. Argonne National Laboratory is operated for the DOE Office of Science by the UChicago Argonne, LLC, under contract no. DE-AC02-06CH11357.

Author contributions

H.W. and X.J. jointly conceived and designed this work. H.C. and H.W. conducted and analyzed the DFT calculations. H.W., Y.M., J.G., T.L., and L.N. performed characterizations and analyzed the obtained data. H.W., N.H., J.H., and X.H. carried out the material synthesis and electrochemical measurements. W.D., G.Z., H.H., D.S., and C.B. gave advice to the research and supervised this work. H.W., T.L., X.J., and K.A. wrote and revised the manuscript, contributed to data analysis, and discussions.

Competing interests

The authors declare no competing interests.

Additional information

Supplementary information The online version contains supplementary material available at <https://doi.org/10.1038/s41467-025-59666-6>.

Correspondence and requests for materials should be addressed to Tongchao Liu, Xiaobo Ji or Khalil Amine.

Peer review information *Nature Communications* thanks Asha Gupta, Zulpiya Shadike, Jin Xie, and the other, anonymous, reviewer for their contribution to the peer review of this work. A peer review file is available.

Reprints and permissions information is available at <http://www.nature.com/reprints>

Publisher's note Springer Nature remains neutral with regard to jurisdictional claims in published maps and institutional affiliations.

Open Access This article is licensed under a Creative Commons Attribution-NonCommercial-NoDerivatives 4.0 International License, which permits any non-commercial use, sharing, distribution and reproduction in any medium or format, as long as you give appropriate credit to the original author(s) and the source, provide a link to the Creative Commons licence, and indicate if you modified the licensed material. You do not have permission under this licence to share adapted material derived from this article or parts of it. The images or other third party material in this article are included in the article's Creative Commons licence, unless indicated otherwise in a credit line to the material. If material is not included in the article's Creative Commons licence and your intended use is not permitted by statutory regulation or exceeds the permitted use, you will need to obtain permission directly from the copyright holder. To view a copy of this licence, visit <http://creativecommons.org/licenses/by-nc-nd/4.0/>.

© The Author(s) 2025